Journal of *Marine Science and Engineering*

MDPI

Article

Seafloor Hydrothermal Activity around a Large Non-Transform Discontinuity along Ultraslow-Spreading Southwest Indian Ridge (48.1–48.7° E)

Dong Chen [1,2], Chunhui Tao [2,3,*], Yuan Wang [2], Sheng Chen [4], Jin Liang [2], Shili Liao [2] and Teng Ding [1]

1 Institute of Marine Geology, College of Oceanography, Hohai University, Nanjing 210098, China; hhuchd@hotmail.com (D.C.); dingteng16@hhu.edu.cn (T.D.)
2 Key Laboratory of Submarine Geosciences, SOA & Second Institute of Oceanography, MNR, Hangzhou 310012, China; wangyuan@sio.org.cn (Y.W.); kamleung@aliyun.com (J.L.); liaosl@sio.org.cn (S.L.)
3 School of Oceanography, Shanghai Jiao Tong University, Shanghai 200240, China
4 Ocean Technology and Equipment Research Center, School of Mechanical Engineering, Hangzhou Dianzi University, Hangzhou 310018, China; chensh@hdu.edu.cn
* Correspondence: taochunhui@sio.org.cn

Abstract: Non-transform discontinuity (NTD) is one category of tectonic units along slow- and ultraslow-spreading ridges. Some NTD-related hydrothermal fields that may reflect different driving mechanisms have been documented along slow-spreading ridges, but the discrete survey strategy makes it hard to evaluate the incidence of hydrothermal activity. On ultraslow-spreading ridges, fewer NTD-related hydrothermal activities were reported. Factors contributing to the occurrence of hydrothermal activities at NTDs and whether they could be potential targets for hydrothermal exploration are poorly known. Combining turbidity and oxidation reduction potential (ORP) sensors with a near-bottom camera, Chinese Dayang cruises from 2014 to 2018 have conducted systematic towed surveys for hydrothermal activity around a large NTD along the ultraslow-spreading Southwest Indian Ridge (SWIR, 48.1–48.7° E). Five new potential hydrothermal anomaly sites (2 inferred and 3 suspected) of high or low temperature and the previously inferred Sudi hydrothermal field occurred in diverse morphotectonic settings along a 78 km long ridge axis. The calculated vent frequency (Fs, sites/100 km) was ~7.7 over the entire study area, higher than the modified value (Fs ≈ 6.5) between 48 and 52° E of SWIR. Even only for the 54 km long large NTD, three hydrothermal anomaly sites yielded an Fs of ~5.6, which is higher than that of most ridge sections and is comparable to some fast-spreading ridges with high-resolution surveys. This indicates that NTDs along ultraslow-spreading ridges could be promising areas in fertilizing hydrothermal activities. Moreover, the deeply penetrating faults on the rift valley walls and strain-focused areas may contribute to the formation of NTD-related hydrothermal circulations. We suggest that NTDs along ultraslow-spreading ridges may be potential targets for further exploration of hydrothermal activities and seafloor sulfide deposits.

Keywords: hydrothermal activity; turbidity and ORP sensors; non-transform discontinuity; ultraslow-spreading ridge; Southwest Indian Ridge

Citation: Chen, D.; Tao, C.; Wang, Y.; Chen, S.; Liang, J.; Liao, S.; Ding, T. Seafloor Hydrothermal Activity around a Large Non-Transform Discontinuity along Ultraslow-Spreading Southwest Indian Ridge (48.1–48.7° E). *J. Mar. Sci. Eng.* **2021**, *9*, 825. https://doi.org/10.3390/jmse9080825

Academic Editor: Dimitris Sakellariou

Received: 21 May 2021
Accepted: 24 July 2021
Published: 30 July 2021

1. Introduction

Seafloor hydrothermal activity occurs along oceanic spreading ridges (OSRs) at various spreading rates [1]. It is a dominant agent in the transfer of energy and material between the inner earth and the ocean, thus playing a key role in the oceanic chemical cycle and supplying energy to deep-sea biological communities as well as the formation of seafloor polymetallic sulfide deposits [2–4]. There is a global trend model showing that the vent spatial frequency is a positive linear function against the spreading rate (that is, the long-term magma budget) of OSRs [1,5,6]. Vent frequency—i.e., the number of vent sites along a 100-km ridge length (Fs, sites/100 km)—is a qualitative index of the

distribution of hydrothermal activity. According to this model, ~400 hydrothermal fields remain undiscovered along slow- (20–55 mm/yr) and ultraslow-spreading (<20 mm/yr) ridges—particularly for the latter, along which ~130 hydrothermal fields will be located, occupying more than 50% of the total sulfide resource of the global mid-ocean ridges (MORs) [2,7].

It has been widely accepted that magmatism and tectonism are two vital factors in controlling the distribution of hydrothermal activity [1,8–10]. On fast and intermediate (>55 mm/yr) OSRs, hydrothermal venting is generally related to the spreading rate and the presence of axial magma chamber beneath the axial volcanic ridges [1,11,12]. On slow and ultraslow OSRs, however, the distribution of hydrothermal activity appears to be more controlled by tectonism due to the more complex geology [9,10,13–17]. Hydrothermal venting fields preferentially occur in axial valley walls and asymmetrically spreading areas where the oceanic spreading is accommodated by tectonic extension [15,18]. In these areas, long-lived downward dipping faults provide necessary conditions for hydrothermal circulations [4,19–21].

Non-transform discontinuity (NTD), characterized by reduced melt supply and accompanied by widespread tectonic activities, is one category of tectonic units along slow and ultraslow OSRs [8,18,22]. Based on the global trend model, NTDs were considered devoid of hydrothermal activity due to their weak thermal budget [5]. However, along the slow-spreading Mid-Atlantic Ridge and Central Indian Ridge, 10 NTD-related hydrothermal fields have in fact been documented on oceanic core complexes massif associated with detachment faults, on volcanic edifices at the central part of NTDs and on off-axis lineament faults [23]. Based on the type of heat source, they may reflect different driving mechanisms, including heat supplied by serpentinization of ultramafic rocks (e.g., Saldanha [24]), by local magmatic sources (e.g., Daxi [23]; Puy des Folles [25]) or by both together (e.g., Rainbow [26]) as well as by residual heat mined from deep crustal and mantle rocks (e.g., Nibelungen [27]). However, the discrete survey strategy makes it hard to evaluate the incidence of hydrothermal activity of NTDs. In contrast to slow OSRs, the size of NTDs along ultraslow OSRs is generally larger due to the more starved magma supply at segment ends and the larger spacing between spreading cells [22,28], and thus they account for a certain fraction of the total ridge length. Due to limited surveys and complicated geological settings, however, only one inactive ultramafic-hosted hydrothermal field on a detachment fault (i.e., Tianzuo [29]) has been confirmed at NTDs along ultraslow OSRs. It remains unclear along ultraslow OSRs which factors contribute to the occurrence of hydrothermal activity at NTDs and whether they could be potential areas in fertilizing hydrothermal activities.

In this study, the detailed hydrothermal exploration results between 48.1 and 48.7° E on a central part of the ultraslow-spreading Southwest Indian Ridge (SWIR) are described. A tectonic unit of NTD is located in this area. Our exploration covered an area of nearly 900 km^2 on rift valleys and ridge flanks by conducting deep-towed survey lines. Evidence for hydrothermal activity was found on the axial rift valley, rift valley wall and ridge flank. Based on these above data, the possible geological processes contributing to the formation of hydrothermal activity are discussed as well as the incidence of hydrothermal activity. These will enrich our understanding of hydrothermal activities on OSR systems and provide indications for hydrothermal investigations and prospecting for seafloor sulfide deposits.

2. Geological Setting

The SWIR, extending ~7700 km from the Bouvet triple junction eastward to the Rodrigues triple junction, is classified as an ultraslow-spreading ridge with a full spreading rate of 12–18 mm/yr [30]. The ridge section between the Indomed and Gallieni Transform Faults (In-Ga TFs) along the SWIR is a first-order supersegment that is offset by a series of NTDs. Based on the position of the center of present magmatic and tectonic activity, Cannat et al. (1999) and Li et al. (2020) divided the Indomed–Gallieni supersegment into

10 second-order segments, numbered 25–34 from east to west [17,31] (Figure 1a). Similar to segments 20–22 (56°40′–52°06′ E) east of the Gallieni TF [22], segments 30–32 alternate with two N45–50° E-trending, deep, 15–20 km wide troughs corresponding to NTDs, which offset the axis by approximately 35 and 32 km, respectively (Figure 1a). Sauter et al. (2001) considered an NTD with an offset larger than 15 km as a large NTD, which is marked by a mantle Bouguer anomaly (MBA) high [22]. Two large NTDs in the oblique ridge section have a length of 54 and 48 km along strike of ridge axis, respectively (Figure 1a).

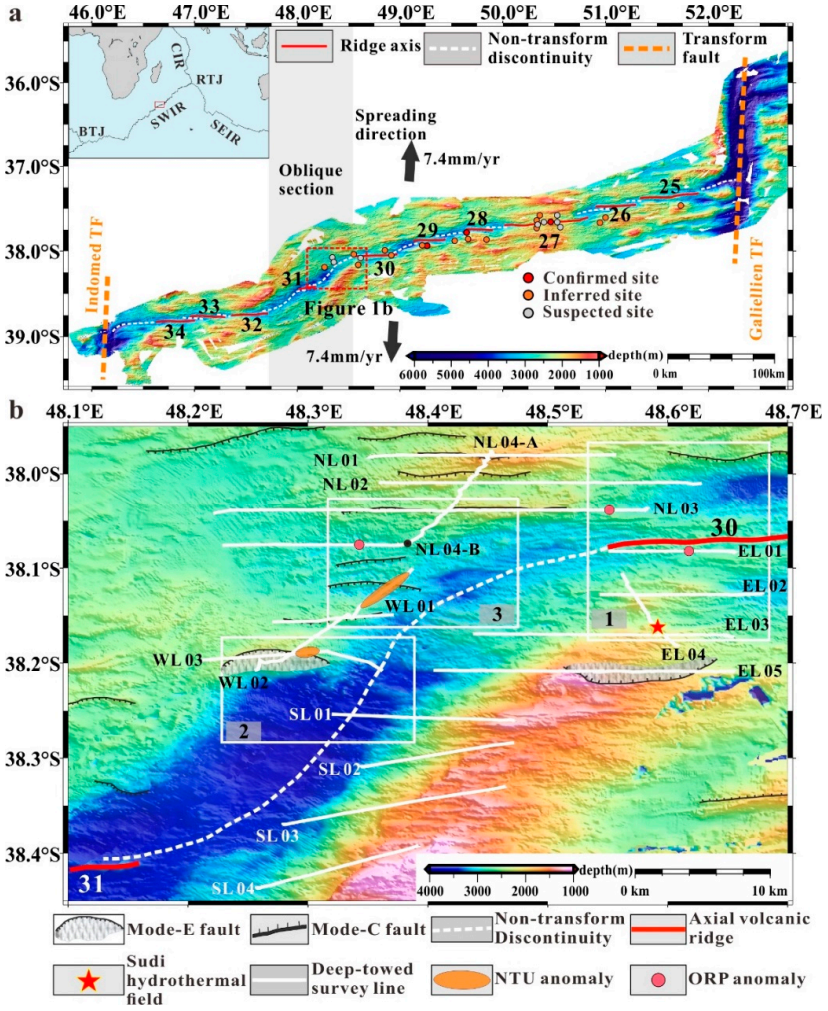

Figure 1. Geological background of our study area on SWIR. (**a**) Bathymetry, segmentation and hydrothermal sites between Indomed and Gallieni TFs. (The bathymetry is from multibeam sonar data by Chinese Dayang cruises.) The top-left inset shows the location between the In-Ga TFs. SWIR: Southwest Indian Ridge; CIR: Central Indian Ridge; SEIR: Southeast Indian Ridge; BTJ: Bouvet triple junction; RTJ: Rodrigues triple junction. (**b**) Detailed bathymetry of our study area. Labels are the names of survey lines, marking the start point (line NL04 is divided into 2 parts owing to the change in heading direction, and the black dot is the turning point). The study area is divided into 4 regions according to the distribution of deep-towed survey lines (i.e., northern, southern, western and eastern regions, marked by the first letter in name of survey line). White boxes with numbers 1, 2 and 3 denote the areas shown in three-dimensional view presented in Figures 7, 8 and 9, respectively. NTU denotes Nephelometric Turbidity Units and ORP denotes the oxidation reduction potential. Note that normal faults are only analyzed from bathymetry data and do not represent entire faults of our study area, and the mode-E faults have greater heaves and spacings than mode-C faults do (the names of these 2 mode faults are simplified from Center-mode fault and Ending-mode fault, which are defined by Benh and Ito, 2008 [32]) (faults data from [33]).

The study area, consisting of the western end of segment 30, the 54 km long large NTD and the eastern end of segment 31 (Figure 1b), is located between segments 30 and 31 (red dotted box in Figure 1a). The ridge axis of the study area is an "S"-shaped strike with rugged terrain (Figure 2). Along the strike of the ridge axis, the study area has a total ridge length of ~78 km, and the water depth varies from ~4000 to 2750 m. The large NTD has an along-axis relief (ΔR) of 1040 m and an MBA variation (ΔMBA) of 66.5 mGal (Figure 2), indicating that there is a significant difference in magma supply. Consequently, the large NTD is further separated into western and eastern parts (Figure 2). There are two localized axial topographic highs with relief around 450–500 m at two ends of segment 30 (48.63° E and 48.82° E) [34], indicating a locally focused melt supply. Liu et al. (2020) identified a series of west–east strike normal faults in our study area by analysis of bathymetry data, including tens of mode-C faults and two mode-E faults, and the latter have greater heaves and spacings [34] (Figure 1b). The previously reported Sudi hydrothermal field (48.6° E) is an inferred field on the southern rift valley wall of segment 30 (Figure 1b) [35].

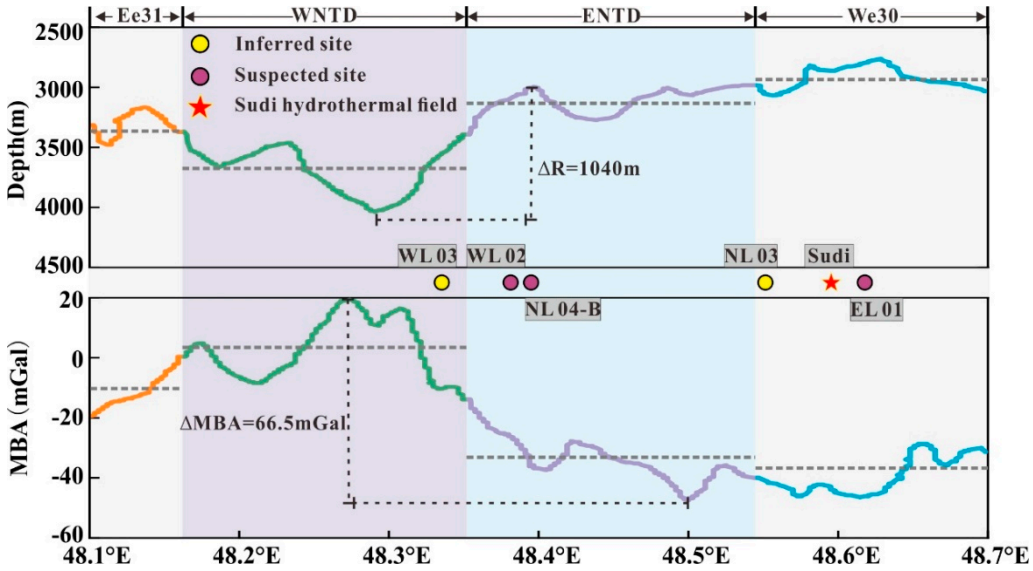

Figure 2. Along-axis topography and MBA of the study area (data from [36]). The profile is separated into 4 sections along the strike of the ridge axis (i.e., along the red lines and the white dotted line): Ee31 marks the eastern end of segment 31, WNTD marks the western part of the large NTD, ENTD is the eastern part of the large NTD and We30 denotes the western end of segment 30. The projection of hydrothermal anomaly sites perpendicular to the ridge axis is shown between 2 panels. Gray dotted lines represent the average value of each section. For clarification and differentiation of suspected sites and inferred sites, see Section 4.2.

3. Data and Methods

During 2014–2018, the 30th, 39th and 49th Chinese Dayang cruises conducted detailed surveys by using a deep-towed hydrothermal detection system (DHDS; [17,37–40]) to explore hydrothermal activity in our study area. In this study, the DHDS employed included a deep-towed body with real-time video, a camera and an ORP sensor, as well as 2–6 Miniature Autonomous Plume Recorders (MAPR) or RBR turbidity sensors (produced by RBR Company) attached along a connected cable within 300 m above the deep-towed body. Sixteen DHDS survey lines with a spacing of 3–5 km covered an area of approximately 900 km^2 between segments 30 and 31. We divided our study area into four regions (i.e., northern, southern, western and eastern regions, marked by the first letter in the name of the survey line in Figure 1b) according to the distribution of these survey lines. In order to collect clear seafloor images, we kept the deep-towed body at 3–5 m altitude, although micro-topographic variations resulted in both collisions with the seafloor and lifting > 5 m altitude occasionally.

The output voltage from the light backscattering sensors of MAPRs or RBRs is directly equivalent to Nephelometric Turbidity Units (NTU) for detecting high-temperature and particle-rich hydrothermal discharge. This type of hydrothermal discharge results in the formation of "black smoker" plume, which can spread several to dozens of kilometers [3,14]. For data preprocessing, we respectively used 2-fold and 10-fold standard deviations as thresholds to remove outliers of raw data twice within a 50-point data window. However, there was still some noise in the data after preprocessing. Following the approach of Goring and Nikora (2002) [41], we constructed an ellipsoid in three-dimensional phase space by using the preprocessed data and the first derivative and second derivative of the preprocessed data. Data points lying outside the ellipsoid were designated as noise and were removed. Then, for the remaining data points, we calculated the 11-point moving averages. Finally, in order to obtain anomalous Nephelometric Turbidity Units (ΔNTU), we subtracted a background value for each MAPR or RBR by calculating an average NTU value of seawater at 500–1500 m depth, which is above the plume depth during each tow.

Data from an ORP sensor can detect dissolved reduced chemical species (e.g., Fe^{+2}, H_2S and H^2) [42] from various hydrothermal discharge types, especially particle-poor low-temperature diffused venting. ORP sensor responses result in an immediate decline in voltage (dE), and the signal generally dissipates within ~1 km from the discharge source, thus providing a more precise location of a discharge source than optical sensors can [3,6]. Owing to the electrode potential drifting of ORP sensors caused by changes in pressure, temperature or electrode recovery following contact with reduced chemicals, raw ORP values sometimes slowly change [3,6,39]; thus, we calculated the derivative of ORP to time (dE/dt) every 25 s to differentiate real anomalies from slowly changing ORP values.

4. Results

4.1. Water Column Anomaly

Referring to the summaries of other hydrothermal vents' anomaly values in the work of Yue et al. (2019) [39], we used NTU and ORP anomalies to identify hydrothermal plumes in our study area. In this paper, an NTU anomaly is a plume spreading more than 1 km with the $\Delta NTU \geq 0.01$. Comprehensive analysis of ORP and dE/dt values is used to identify ORP anomalies [11]. An ORP anomaly is defined as an overall decrease larger than 2 mv for any measurement of ORP value during consecutive measurements, with a rate of decline (dE/dt) > 0.04 mv/s, that then begins a lengthy recovery [3]. Accordingly, the whole path of an ORP anomaly response is a curve in sharp decline followed by an upward trend, which results in a distinct downward tip [38,39]. Furthermore, multiple ORP responses within 1 km are considered to result from a single discharge source [3]. Based on analysis of the NTU and ORP data, no water column anomaly was revealed in the southern region, while two NTU and three ORP isolated anomalies from each other were identified along 5 of the 12 DHDS survey lines (i.e., lines NL03, NL04-B, EL01, WL02 and WL03) in the other three regions (Figure 1b). Some ORP anomalies related to the hitting on the seafloor of the towed body were excluded (orange dotted ellipses in Figure 3).

Four DHDS survey lines covered the northern region (Figure 1b). Based on the mapping of plumes, no NTU anomaly was detected except for one ORP anomaly each along lines NL03 and NL04-B (Figure 3a,b). The plume NL03 has two obviously decreased values in ORP (dE/dt) of −0.14 and −0.15 mv/s within 1 km, with ΔNTU values < 0.003 (Figure 3a). Only one ORP (dE/dt = −0.32 mv/s) drop of 5.37 mv is found around 48.34° E at a depth of ~2800 m along line NL04-B, although a ΔNTU value of approximately 0.007 presents in the whole mid-water layer (2600–2900 m) (Figure 3b).

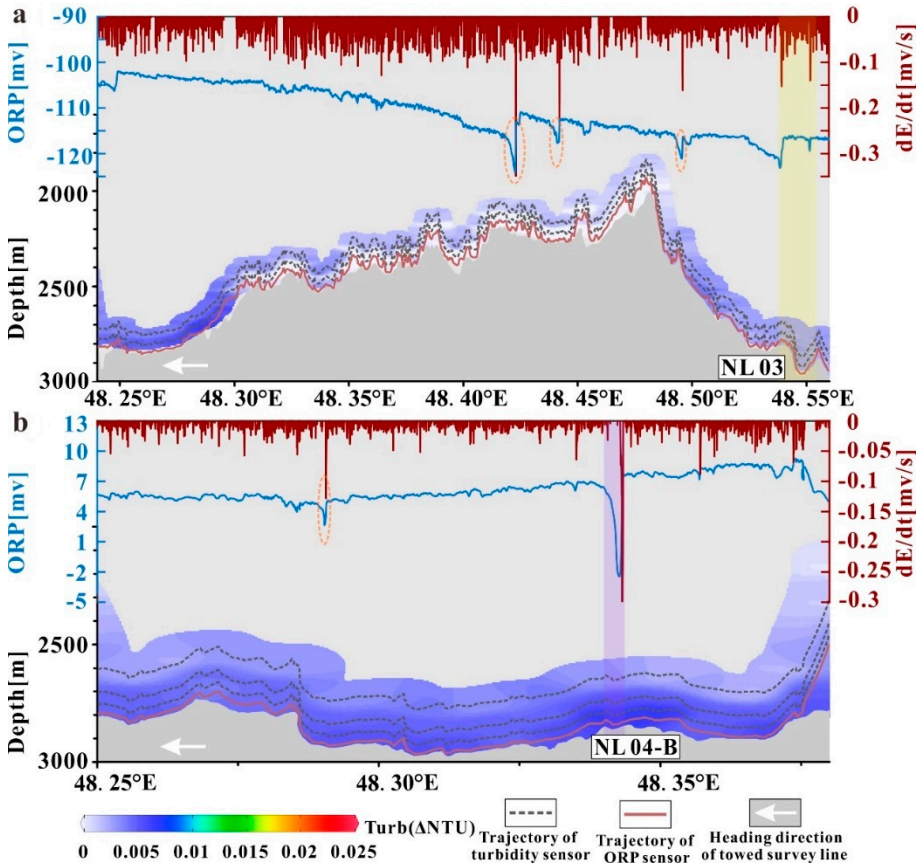

Figure 3. Hydrothermal plume distribution along DHDS lines. (**a**,**b**) The seafloor relief, ΔNTU, ORP and negative dE/dt along lines NL03 and NL04-B, respectively. The top blue line is ORP and the top brown line is dE/dt. Note that the orange dotted ellipses are the incorrect records from the ORP sensor caused by the towed body hitting the seafloor. The yellow band indicates an inferred hydrothermal anomaly site, and the purple band indicates a suspected one. Both panels use the same colorbar and legend.

In the eastern region, five DHDS survey lines were conducted to detect hydrothermal activity (Figure 1b). Only one ORP anomaly was found along line EL01; the plume has a decreased ORP (dE/dt = −0.18 mv/s) value of 5.36 mv (Figure 4). The Sudi hydrothermal field is an inferred field [35]; however, the nearby ORP and turbidity data of the DHDS survey lines do not reveal apparent anomalies (Figure 1b).

Different from the above two regions, the analyses of NTU and ORP data from survey lines in the western region only revealed two NTU anomalies along lines WL02 and WL03 (Figures 1b and 5a,b). The WL02 plume, without an ORP anomaly, continuously spread more than 4 km with a maximum ΔNTU value of nearly 0.04; however, the plume rising height was only restricted to 60 m above the seafloor at a water depth ranging from ~2800 to 3000 m (Figure 5b,d). As for the plume WL03, only the uppermost RBR (300 m above the towed body) recorded an obvious NTU anomaly reaching 0.07 ΔNTU at a center depth of ~2000 m, extending ~1.8 km from west to east (Figure 5a,c).

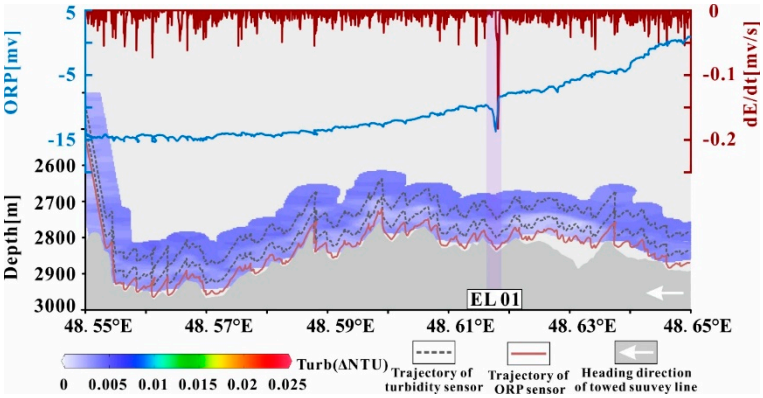

Figure 4. Hydrothermal plume distribution along line EL01. The seafloor relief, ΔNTU, ORP and negative dE/dt are shown. The top blue line is ORP and the top brown line is dE/dt. The purple band indicates a suspected hydrothermal anomaly site.

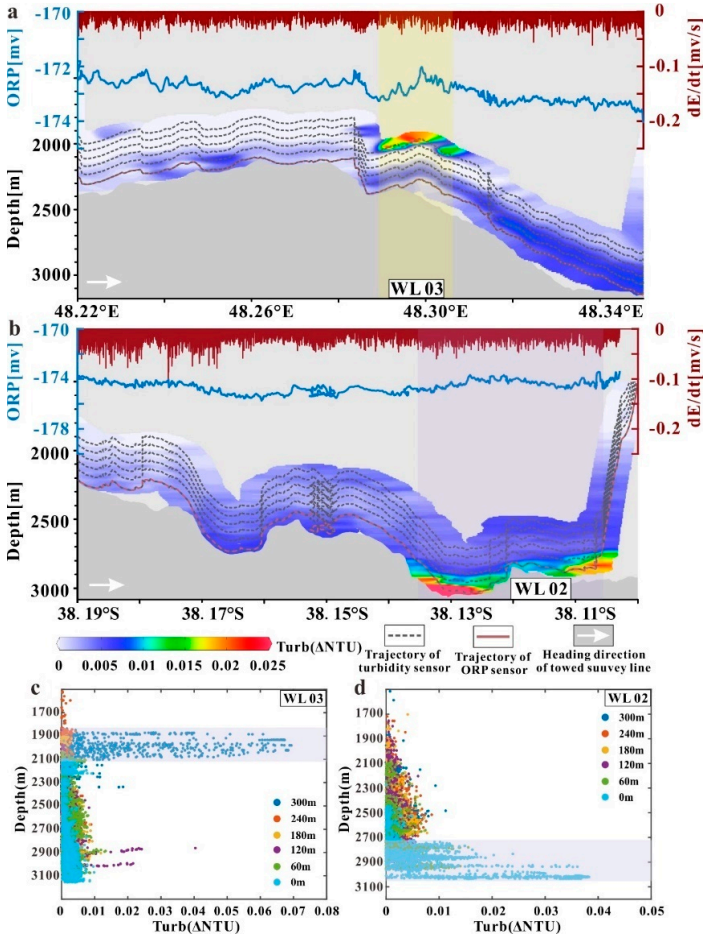

Figure 5. Horizontal and vertical distribution of hydrothermal plume along DHDS lines. (**a**,**b**) The seafloor relief, ΔNTU, ORP and negative dE/dt along lines WL03 and WL02, respectively. The top blue line is ORP and the top brown line is dE/dt. The yellow band indicates an inferred hydrothermal anomaly site, and the purple band indicates a suspected one. Both panels use the same colorbar and legend. (**c**,**d**) The vertical ΔNTU variation of lines WL03 and WL02, respectively; dots in various colors represent different heights of turbidity sensors above the towed body. The transparent band marks the depth layer of NTU anomaly.

4.2. Category and Reliability of Hydrothermal Anomaly Sites

Compared to the surrounding seawater, hydrothermal plumes are rich in metallic elements (e.g., Fe, Mn and Zn) and suspended particles (e.g., sulfides and oxyhydroxides) and have higher temperatures [3,38,39,43–46]. Furthermore, hydrothermal altered rocks, metalliferous sediments, consolidated carbonate sediments (called "seabed types anomaly" in the paper of Yue et al., 2019 [39]) and fauna around vents are apparently different from usual seafloor [47]. Tracers used for detecting hydrothermal plumes in the water column, such as turbidity, ORP, temperature and dissolved Mn, Fe, CH_4, H_2S and ^3He [3], together with seabed types and hydrothermal vent fauna are the common criteria used to determine the locations of hydrothermal fields and to identify the types (high-temperature focused or low-temperature diffused) of hydrothermal discharge sites [37,48].

Here, by combing the characteristics of observed plumes with the recorded seafloor images below them, we could infer the types of hydrothermal discharge sites that the five newly identified water column anomalies derived from. As no vents or typical hydrothermal products were observed, we used "suspected site" and "inferred site" to clarify the reliability of our evidence to infer hydrothermal anomaly sites. Table 1 provides detailed information of each site.

Table 1. Information of water column anomaly and seafloor surface.

Site Name	Site Type	Seafloor Surface Description	Longitude (°E)	Latitude (°N)	Observed Plume Length (km)	Plume Rise Height (m)	NTU Anomaly (ΔNTU)	ORP Anomaly (mV)	dE/dt (mv/s)
NL03	Inferred low-temperature diffused site	Fragments of pillow lavas, consolidated carbonate sediments	48.55	−38.04	-	-	-	−2.91	−0.14
			48.54	−38.04	-	-	-	−6.58	−0.15
NL04-B	Suspected low-temperature diffused site	Pelagic sediments	48.34	−38.08	-	-	-	−5.37	−0.32
EL01	Suspected low-temperature diffused site	Pillow lavas	48.61	−38.08	-	-	-	−5.36	−0.18
WL02	Suspected low-temperature diffused site	Pelagic sediments	48.36	−38.13	4.3	0–60	0.01–0.04	-	-
WL03	Inferred high-temperature focused site	Breccia or debris	48.30	−38.19	1.8	>300	0.01–0.07	-	-

4.2.1. Suspected Sites

In this study, a suspected site is supported by evidence of an OPR-only anomaly or by evidence of a weak NTU-only anomaly (i.e., plume rising height < 100 m and maximum ΔNTU value < 0.04; [38,39]).

Site NL04-B (48.34° E/38.08° S) and site EL01 (48.61° E/38.08° S) are considered as two suspected low-temperature diffused sites. The ORP-only anomaly implies that a low-temperature diffused fluid flow generated from a low-temperature discharge source may exist around each site (generally within 1 km) (Figures 3b and 4) [3,11,47,49]. Recorded images of the seafloor show mainly sediments at site NL04-B (Figure 6a) and pillow lavas with few sediments cover at site EL01 (Figure 6b), and direct evidence related to typical low-temperature hydrothermal activity was not observed.

Site WL02 is provisionally located at 48.36° E/38.13° S, where the 4.3 km long NTU anomaly has the maximum ΔNTU value (Figure 5b). The seafloor underlying the NTU anomaly is primarily covered by sediments (Figure 6c), though a few pillow lavas and breccia with sediment cover were occasionally seen on steep slopes or in fractures. The lowest RBR (on the towed body) recorded a maximum ΔNTU value of ~0.04, and therefore, we cannot rule out the influence of the resuspended bottom sediments. However, the

RBR at 60 m altitude also recorded an NTU anomaly of ~0.015 ΔNTU (Figure 5d), and we inferred that this NTU anomaly may result from a discharge source with low heat flux 1 km away. As a result, site WL02 is designated as a suspected low-temperature diffused site.

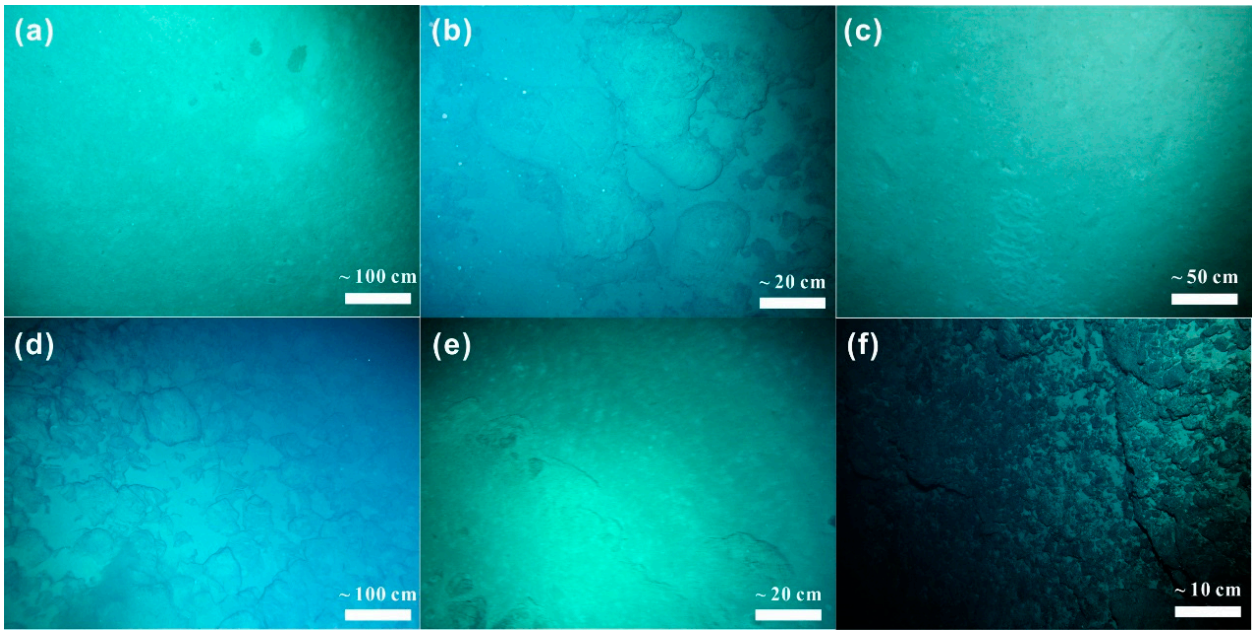

Figure 6. Typical seafloor photos below observed plumes. (**a**) Pelagic sediments below NL04-B plume. (**b**) Pillow lavas with few sediments cover below EL01 plume. (**c**) Pelagic sediments below WL02 plume. (**d**) Fragments of pillow lavas with sediment cover and (**e**) consolidated carbonate sediments below NL03 plume. (**f**) Breccia/debris with few sediments cover below WL03 plume.

4.2.2. Inferred Sites

In this study, an inferred site is supported by evidence of a significant NTU-only anomaly (i.e., plume rising height > 150 m and ΔNTU value > 0.01; [38,39]) or by evidence of an ORP-only anomaly accompanied by a possible seabed anomaly.

Site NL03 is regarded as an inferred low-temperature diffused site. The detected ORP-only anomaly with two potential drops between 48.54° E and 48.55° E implies that a diffused fluid flow may be present (Figure 3a). Recorded images below the anomaly primarily show fragments of pillow lavas with sediment cover (Figure 6d). However, consolidated carbonate sediments (Figure 6e) that may be associated with a low-temperature hydrothermal process [50,51] were observed at 48.55° E.

The NTU anomaly from site WL03 was only detected by the uppermost RBR at a depth of 1900–2100 m, which is more than 300 m above the seafloor (Figure 5a,c). The true thickness of the hydrothermal plume and the location of its source are uncertain. The observed plume in the western NTD is exactly above the top of the rift valley wall where a south-facing mode-E fault was identified by Liu et al. (2020) [33] (Figure 1b). This mode-E fault has a length of ~11 km and a heave of ~2.5 km, and the depth of its fault plane ranges from 2200 to 2800 m (Figure 1b). Recorded images of the seafloor along the mode-E fault are mainly breccia/debris with few sediments (Figure 6f), which is consistent with the analysis of Liu et al. (2020) [33]. This indicates that the area has relatively higher permeability generated by tectonic activity and is favorable for hydrothermal activity. Owing to the rising height of the detected NTU anomaly >300 m, we inferred that it results from a typical high-temperature "black smoker" plume whose source has a higher heat flux [3,11,17,38]. Generally, the rising height of a "black smoker" plume is no more than 500 m above the seafloor [11,14,17,49,52–54]. According to the depth range of the detected NTU anomaly, the inferred depth of its source ranges from ~2000 to 2500 m, which bins in the depth range of the fault plane. Consequently, the discharge source of the observed plume is more likely

located on the mode-E fault plane. We consider site WL03 as an inferred high-temperature focused site and momentarily located it at 48.3° E/38.19° S, below the observed plume.

5. Discussion

5.1. Geological Processes Contributing to Formation of Hydrothemal Activities

The SWIR is characterized by a starved magma supply; however, locally enhanced magmatism caused by focused melt injection and sufficient permeability generated by tectonic activity provide conditions to drive hydrothermal circulation [9]. The confirmed hydrothermal fields along the SWIR occur on segment centers, including Duanqiao [55], Tiancheng [56] and Mount Jourdanne [57], and on detachment faults of the rift valley walls, including Yuhuang [58], Longqi [9] and Tianzuo [29]. Our newly inferred hydrothermal anomaly sites based on plume mapping and the previously reported SDF occupy various morphotectonic settings (white boxes in Figure 1b) around the large NTD area (Figures 7–9).

5.1.1. Hydrothermal Activity on Western End of Segment 30

Three hydrothermal anomaly sites (i.e., NL03, EL01 and SDF) are located on the western end of segment 30 (Figures 1b and 7). Two low-temperature diffused sites, namely site NL03 (~4.6 km off-axis) and site EL01, are situated on an axial volcanic zone (Figure 7). A previous study assumed that low-temperature diffused venting predominantly occurs in association with high-temperature venting [59], whereas our detection of a water column anomaly around this area does not reveal any information related to high-temperature venting. We thus infer that these two low-temperature diffused sites are isolated diffused venting. Isolated low-temperature diffused venting seems to not be uncommon along ridge crests, which is supported by seafloor observations [3,6]. These include seawater mixing with upwelling hydrothermal fluids within porous erupted volcanic layers as well as systems evolving from high- to low-temperature discharge [60–62]. For the first scenario, isolated low-temperature diffused venting seems to be governed by episodic volcanic eruptions on regions with a thickened crust (~10 km) (e.g., Lilliput field [63]) or with strong melt supply, such as a fast-spreading ridge [3,61], because a highly ductile crust with a few deep fractures on these regions obstructs the seawater from reaching deep enough to be heated adequately [47,63]. Taking the western end of segment 30 into consideration, the first scenario could be precluded for an average crustal thickness of only ~5.9 km [36]. Therefore, the two isolated low-temperature diffused hydrothermal activities may be the result that previously existed hydrothermal systems have evolved from high to low temperature. On the eastern end of segment 30, due to the locally focused melt supply, a high-temperature hydrothermal plume has been identified [17,34]. Similarly, the locally focused melt supply on the western end of segment 30 appears to provide a moderate heat source for driving the hydrothermal circulation, although the melt supply may have decreased to a present waning state. In addition, the SDF (~9.4 km off-axis) is situated on the southern axial valley wall (Figure 7b)—this location is consistent with many vent fields that are controlled by rift-bounding faults along slow- and ultraslow-spreading ridges [10,19,21,64]. Consequently, we infer that the rift-bounding fault may be activated by the locally focused melt supply and, therefore, act as pathway for channeling hydrothermal fluids to off-axis areas [17,39].

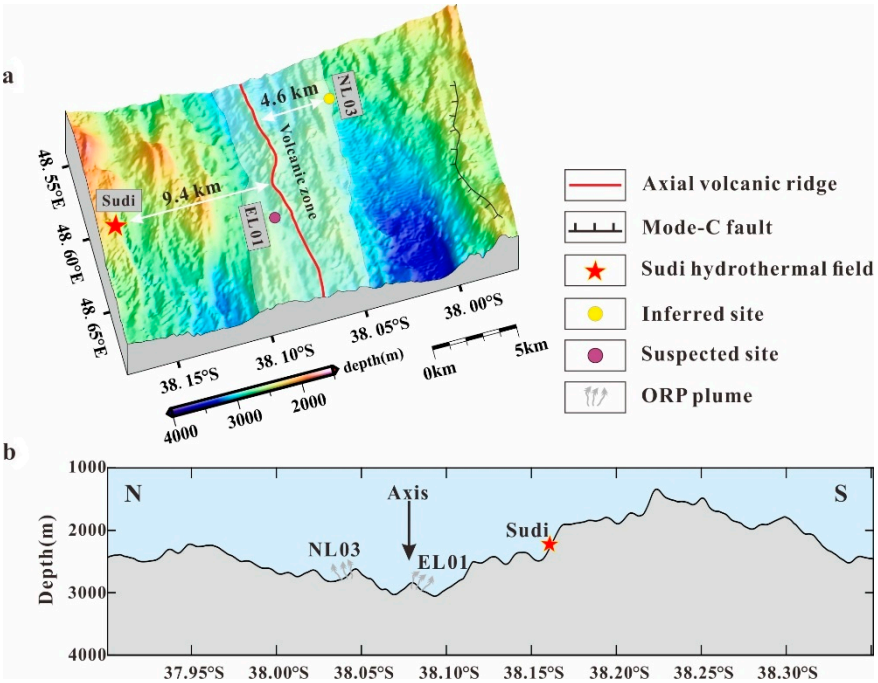

Figure 7. Distribution of hydrothermal anomaly sites for the western end of segment 30. (**a**) Distribution of hydrothermal anomaly sites in three-dimensional view. The transparent area indicates the axial volcanic zone. (**b**) Distribution of hydrothermal anomaly sites in schematic profile perpendicular to the ridge axis.

5.1.2. Hydrothermal Activity on the Western NTD

Site WL03 is situated at the top of the northern rift valley wall of the western NTD (white box with number of 2 in Figure 1b) and ~6.7 km off-axis (Figures 2 and 8). Similar to the Taiji hydrothermal field [65], site WL03 also occurs on an off-axis lineament fault dipping into the NTD (Figure 8a). The ~2.7-km average axial crustal thickness of the western NTD [36] indicates an area of significantly diminished magmatism, which is responsible for the cooler and thicker lithosphere [30,66]. Conventionally, a cooler and thicker lithosphere beneath this area would increase the depth of mantle partial melting and, thus, retard the upwelling of magma from the melt injection zone (i.e., brittle–ductile transition zone), and this area is expected to be devoid of hydrothermal activity due to the weak thermal supply [5]. Under this circumstance, we propose that the mode-E fault (Figure 8a) might be the dominant controlling factor for the high-temperature hydrothermal activity in this area.

In a study of young off-axis volcanism on an oblique spreading amagmatic segment of SWIR, Standish and Sims (2010) suggested that although the cooler and thicker lithosphere caused the brittle–ductile transition zone to be deeper, the depth to which faults penetrate would deepen as well. Therefore, the faults are likely to reach the melt injection zone and provide pathways for the transportation of melt [67]. Moreover, numerical modeling of the spreading environments where more than 50% of the accretion is accommodated by tectonic extension (i.e., the fraction of magmatic accretion M < 0.5) also shows that long-lived, large-offset normal faults can extend far away from the axis and are often rooted in the brittle–ductile transition zone [68]. Liu et al. (2020) measured the fraction of magmatic accretion, M, and the depth of rift valley, D, of each segment between the In-Ga TFs, and the M and D in the northern flank of the western NTD are 0.38 and ~1.1 km, respectively (segment 5 in that study) [33]. According to the analysis of Liu (2019) [36], this mode-E fault with a heave of ~2.5 km and a D of ~1.1 km is continuously slipping. On this basis, we infer that this mode-E fault may extend into the melt injection zone beneath the western NTD, thus being the pathway for the high-temperature hydrothermal circulation. It has

been widely acknowledged that a heat source of magmatic origin is required to sustain high-temperature hydrothermal circulation [69]. In a detachment faulting system in the Dragon Horn area (49.7° E on SWIR), Tao et al. (2020) revealed a deep high-temperature hydrothermal circulation that is ~6 km deeper than the Moho boundary and proposed that the melt zone in the lithospheric mantle might be the magmatic heat source [50]. In addition, within extension-dominated rift valleys, fault-aided melt flow along pre-existing fractures can supply ample magma to crustal levels, resulting in thick gabbro sections within the footwalls of high-angle faults [70,71]. In summary, it could be possible that the high-temperature hydrothermal circulation is maintained by the cooling of gabbro sections and melt directly transported from the melt injection zone along the deeply penetrating mode-E fault [14], or the deeply penetrating mode-E fault may provide a permeable pathway that permits the access of seawater to the melt zone in lithospheric mantle, as with the high-temperature hydrothermal circulation in the Dragon Horn area [50].

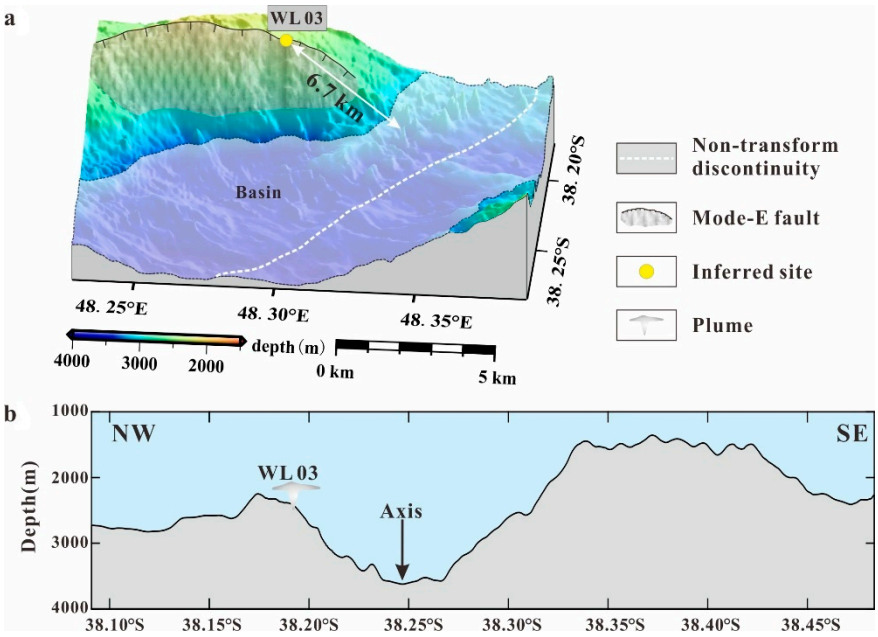

Figure 8. Location of site WL03 for the western NTD. (**a**) Three-dimensional view around site WL03. The transparent area indicates an axial basin. (**b**) Location of site WL03 shown in schematic profile perpendicular to the ridge axis.

5.1.3. Hydrothermal Activity on the Eastern NTD

Two suspected low-temperature diffused sites (Figures 2 and 9) are located in the northwest flank area of the eastern NTD (white box with number of 3 in Figure 1b). Sites NL04-B and WL02 are about 10.1 and 3.4 km off-axis of the eastern NTD, respectively, and surrounded by several mode-C faults (Figure 9a). Studies along the CIR (8–17° S) have shown that diffused venting is expected to be common on fault zones of ridge flanks (up to 10 km off-axis) [10,64]. Similar to fault zones on the flanks of the Central Indian Ridge, the mode-C faults in this area may facilitate the seepage of seawater. However, the heat source sustaining the two low-temperature hydrothermal activities is ambiguous. In terms of the average along-axis MBA value of each section shown in Figure 2, the value of the eastern NTD is merely 3.6 mGal higher than that of the western end of segment 30, indicating that they may have a similar level of melt supply. The magma supply beneath the western end of segment 30 may now be at a waning stage as discussed above, and it may be the same beneath the eastern NTD. Under the circumstance of waning magma supply, there may be some geological process that can help to provide the needed heat to drive the hydrothermal circulation in the northwest flank area. On the basis of a teleseismic focal mechanism solution, this area is in a state of shear deformation and corresponds to a

strain-focused area [72]. Numerical modeling of the strain distribution on ridge sections oblique to the spreading direction has shown that a strain-focused area may be conducive to the focus of magma supplied by the melt injection zone towards itself in the crustal level [73]. We infer that this process may focus the melt to the northwest flank area of the eastern NTD, therefore providing moderate heat for the two hydrothermal activities. Additionally, the reduced magma supply beneath the eastern NTD can possibly now only sustain low-temperature diffused hydrothermal activity, as with the western end of segment 30.

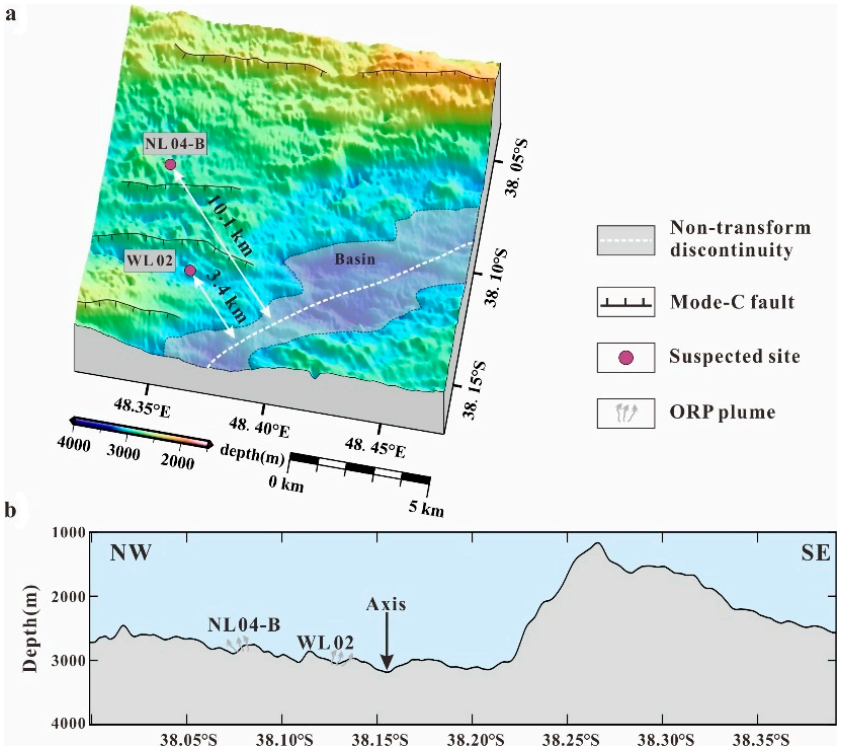

Figure 9. Distribution of hydrothermal anomaly sites for northwest flank of the eastern NTD. (**a**) Distribution of hydrothermal anomaly sites in three-dimensional view. The transparent area indicates an axial basin. (**b**) Distribution of hydrothermal anomaly sites in schematic profile perpendicular to the ridge axis.

5.2. Hydrothermal Vent Frequency (Fs)

Previous results of detailed surveys combing the use of optical and ORP sensors have shown that the incidence of hydrothermal activity was underestimated between the In-Ga TFs along the SWIR [17,39].

To evaluate the incidence of hydrothermal activity in this study, we used the total measured length of 78 km as the survey length to calculate the vent frequency (sites/100 km) of the entire study area, while the measured length of 54 km (white dotted line in Figure 1b) was used only for the large NTD area. The full spreading rate of our study area is 12.2 mm/y (from InterRidge Database), and thus, the expected Fs would be 1.1 as calculated by the global trend model [6,7]. For the entire study area, the total of six hydrothermal sites yielded an Fs value of ~7.7 (red star in Figure 10), which is ~7-fold the expected Fs value. If we only take the large NTD area into consideration, three hydrothermal anomaly sites (NL04-B, WL02 and WL03) would yield an Fs value of ~5.6 (red triangle in Figure 10), which is significantly higher than the expected Fs value. By integrating our results with previously reported hydrothermal activities between 48 and 52° E of the SWIR, 26 hydrothermal sites (3 confirmed, 15 inferred and 8 suspected) [9,17,35,39,55,74] along the 404 km long ridge axis yielded a modified Fs value of ~6.5 (purple diamond in Figure 10), which is lower than that of our entire study area. In this study, four of six hydrothermal sites occurred

on down-dipping faults of rift valley walls and shear deformation areas on the northwest flank of the eastern NTD, indicating that the distribution of hydrothermal activity may be more controlled by tectonism. Significantly, the Fs value of the large NTD is higher than that of most of ridge sections and is even comparable to some fast-spreading ridges with high-resolution surveys (Figure 10) [3]. This indicates that the NTDs along ultraslow-spreading ridges may also be potential areas in fertilizing hydrothermal activities, and the deeply penetrating faults on rift valley walls and strain-focused areas may contribute to the formation of NTD-related hydrothermal circulation.

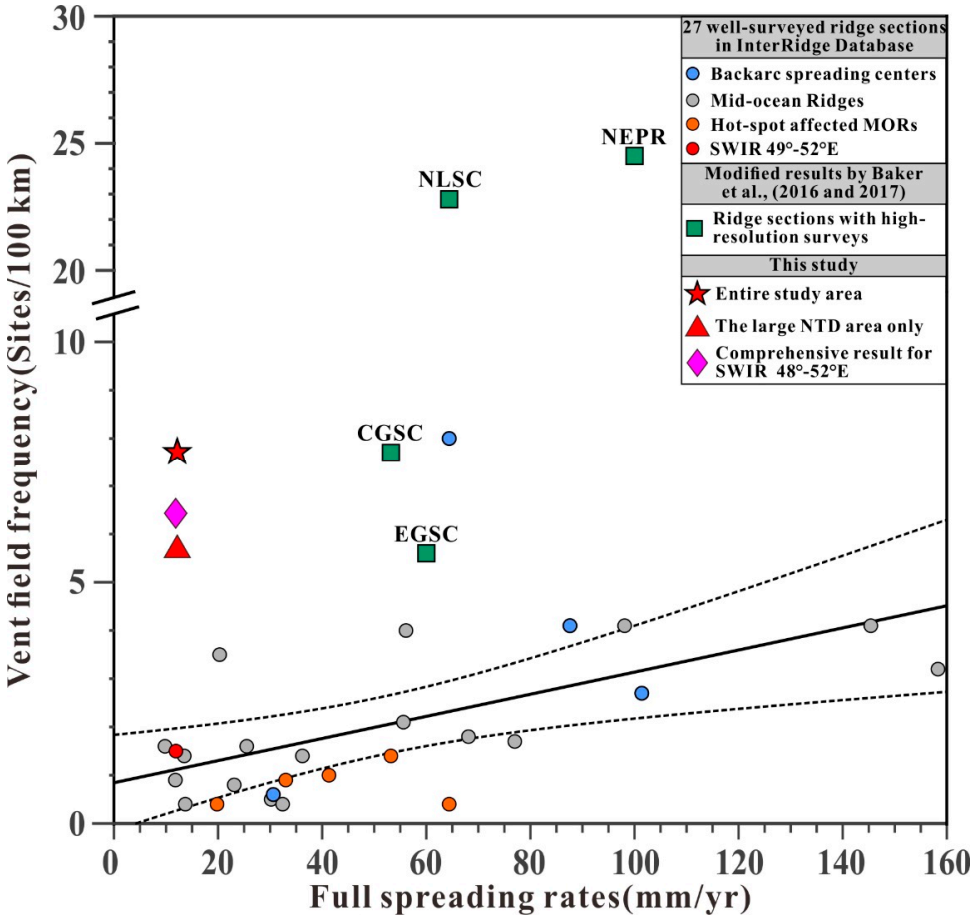

Figure 10. Vent field spatial frequency (Fs) versus full spreading rate of OSR sections. Circles represent 27 well-surveyed ridge sections spanning the entire range of spreading rates (data from www.vent-data.interridge.org/; accessed on 25 March 2020). Green squares represent modified values of ridge sections with high-resolution surveys [3]. CGSC is the Central Galapagos Spreading Center, EGSC is the Eastern Galapagos Spreading Center, NLSC is the Eastern Lau Spreading Center and NEPR is the Northern East Pacific Rise. The red star denotes our entire study area, the red triangle represents the large NTD area in this study and the purple diamond is the modified value for the ridge section between 48 and 52° E of the SWIR (comprehensive results of our study and previously published reports). The black line is the linear regression trend using the 27 well-surveyed ridge sections, and black dotted curves are ±95% confidence intervals. This figure is modified from [6,7].

6. Conclusions

We conducted a systematic hydrothermal exploration to seek evidence of seafloor hydrothermal activity around the large NTD along the ultraslow-spreading SWIR between the In-Ga TFs. In addition to the inferred Sudi hydrothermal field, four low-temperature diffused sites (1 inferred and 3 suspected) and one inferred high-temperature focused site were newly inferred to occur in diverse morphotectonic settings. The inferred high-

temperature focused site provides new evidence of high-temperature hydrothermal activity at NTDs along ultraslow-spreading ridges. Six hydrothermal sites in the entire study area yielded a vent frequency (Fs) of ~7.7, higher than the modified value for 48–52° E of the SWIR (Fs ≈ 6.5). Even only for the large NTD area, the inferred high-temperature focused site situated on a deeply penetrating mode-E fault of the rift valley wall and two suspected low-temperature diffused sites occurring on a strain-focused area yielded an Fs value of 5.6, higher than that of most ridge sections, and is comparable to some fast-spreading ridge sections with high-resolution surveys. Deeply penetrating faults on rift valley walls and strain-focused areas may contribute to the formation of NTD-related hydrothermal activities along ultraslow-spreading ridges. We suggest that NTDs along ultraslow-spreading ridges may also be further potential targets for hydrothermal exploration.

Author Contributions: Conceptualization, D.C. and C.T.; methodology, Y.W. and S.C.; validation, C.T.; formal analysis, D.C. and C.T.; investigation, C.T.; resources, C.T.; data curation, D.C.; writing—original draft preparation, D.C.; writing—review and editing, J.L., S.L. and T.D.; visualization, D.C.; supervision, C.T. and Y.W.; project administration, C.T.; funding acquisition, C.T. All authors have read and agreed to the published version of the manuscript.

Funding: This work was funded by the National Key R&D Program of China under contract No. 2018YFC0309901 and No. 2017YFC0306203; the Scientific Research Fund of the Second Institute of Oceanography, MNR under contract No. JG1905; the COMRA Major Project under contract No. DY135-S1-01-01 and No. DY135-S1-01-09; the National Natural Science Foundation of China under contract No. 42006167 and No. 41806076, and the Natural Science Foundation of Zhejiang Province under contract No. LQ19D060008.

Institutional Review Board Statement: Not applicable.

Informed Consent Statement: Not applicable.

Data Availability Statement: The data used to support the findings of this study are available from the corresponding author upon request.

Acknowledgments: We thank the Science Party, the captains and the crew of the 30th, 39th and 49th COMRA DY Cruises. We thank the reviewers and the editor for their thoughtful reviews.

Conflicts of Interest: The authors declare no conflict of interest.

References

1. Baker, E.T.; German, C.R. On the global distribution of hydrothermal vent fields. Mid-Ocean Ridges: Hydrothermal Interactions between the Lithosphere and Oceans. *Geophys. Monogr. Ser.* **2004**, *148*, 245–266.
2. Hannington, M.; Jamieson, J.; Monecke, T.; Petersen, S.; Beaulieu, S. The abundance of seafloor massive sulfide deposits. *Geology* **2011**, *39*, 1155–1158. [CrossRef]
3. Baker, E.T.; Resing, J.A.; Haymon, R.M.; Tunnicliffe, V.; Lavelle, J.W.; Martinez, F.; Ferrini, V.; Walker, S.L.; Nakamura, K. How many vent fields? New estimates of vent field populations on ocean ridges from precise mapping of hydrothermal discharge locations. *Earth Planet. Sci. Lett.* **2016**, *449*, 186–196. [CrossRef]
4. German, C.R.; Petersen, S.; Hannington, M.D. Hydrothermal exploration of mid-ocean ridges: Where might the largest sul-fide deposits be forming? *Chem. Geol.* **2016**, *420*, 114–126. [CrossRef]
5. Baker, E.T.; Chen, Y.J.; Morgan, J. The relationship between near-axis hydrothermal cooling and the spreading rate of mid-ocean ridges. *Earth Planet. Sci. Lett.* **1996**, *142*, 137–145. [CrossRef]
6. Baker, E. Exploring the ocean for hydrothermal venting: New techniques, new discoveries, new insights. *Ore Geol. Rev.* **2017**, *86*, 55–69. [CrossRef]
7. Beaulieu, S.E.; Baker, E.T.; German, C.R. Where are the undiscovered hydrothermal vents on oceanic spreading ridges? *Deep. Sea Res. Part II Top. Stud. Oceanogr.* **2015**, *121*, 202–212. [CrossRef]
8. German, C.; Parson, L. Distributions of hydrothermal activity along the Mid-Atlantic Ridge: Interplay of magmatic and tectonic controls. *Earth Planet. Sci. Lett.* **1998**, *160*, 327–341. [CrossRef]
9. Tao, C.; Lin, J.; Guo, S.; Chen, Y.J.; Wu, G.; Han, X.; German, C.R.; Yoerger, D.R.; Zhou, N.; Li, H.; et al. First active hydrothermal vents on an ultraslow-spreading center: Southwest Indian Ridge. *Geology* **2012**, *40*, 47–50. [CrossRef]
10. Son, J.; Pak, S.-J.; Kim, J.; Baker, E.T.; You, O.-R.; Son, S.-K.; Moon, J.-W. Tectonic and magmatic control of hydrothermal activity along the slow-spreading Central Indian Ridge, 8° S–17° S. *Geochem. Geophys. Geosystems* **2014**, *15*, 2011–2020. [CrossRef]

11. Baker, E.T.; Hémond, C.; Briais, A.; Maia, M.; Scheirer, D.S.; Walker, S.L.; Wang, T.; Chen, Y.J. Correlated patterns in hydro-thermal plume distribution and apparent magmatic budget along 2500 km of the Southeast Indian Ridge. *Geochem. Geophys. Geosystems* **2014**, *15*, 3198–3211. [CrossRef]
12. Baker, E.T. Relationships between hydrothermal activity and axial magma chamber distribution, depth, and melt content. *Geochem. Geophys. Geosystems* **2009**, *10*, 10. [CrossRef]
13. German, C.R.; Baker, E.T.; Mevel, C.; Tamaki, K. Hydrothermal activity along the southwest Indian ridge. *Nat. Cell Biol.* **1998**, *395*, 490–493. [CrossRef]
14. Baker, E.T.; Edmonds, H.N.; Michael, P.J.; Bach, W.; Dick, H.J.; Snow, J.E.; Walker, S.L.; Banerjee, N.R.; Langmuir, C.H. Hydrothermal venting in magma deserts: The ultraslow-spreading Gakkel and Southwest Indian Ridges. *Geochem. Geo-Phys. Geosystems* **2004**, *5*, 1–29.
15. Escartín, J.; Smith, D.K.; Cann, J.; Schouten, H.; Langmuir, C.H.; Escrig, S. Central role of detachment faults in accretion of slow-spreading oceanic lithosphere. *Nat. Cell Biol.* **2008**, *455*, 790–794. [CrossRef] [PubMed]
16. Bach, W.; Banerjee, N.R.; Dick, H.J.B.; Baker, E.T. Discovery of ancient and active hydrothermal systems along the ultra-slow spreading Southwest Indian Ridge 10°–16° E. *Geochem. Geophys. Geosystems* **2002**, *3*, 1–14. [CrossRef]
17. Li, H.; Tao, C.; Yue, X.; Baker, E.T.; Deng, X.; Zhou, J.; Wang, Y.; Zhang, G.; Chen, J.; Lü, S.; et al. Enhanced hydrothermal activity on an ultraslow-spreading supersegment with a seismically detected melting anomaly. *Mar. Geol.* **2020**, *430*, 106335. [CrossRef]
18. Gràcia, E.; Charlou, J.L.; Radford-Knoery, J.; Parson, L.M. Non-transform offsets along the Mid-Atlantic Ridge south of the Azores (38° N–34° N): Ultramafic exposures and hosting of hydrothermal vents. *Earth Planet. Sci. Lett.* **2000**, *177*, 89–103. [CrossRef]
19. McCaig, A.; Cliff, R.A.; Escartin, J.; Fallick, A.; MacLeod, C. Oceanic detachment faults focus very large volumes of black smoker fluids. *Geology* **2007**, *35*, 935. [CrossRef]
20. Pak, S.-J.; Moon, J.-W.; Kim, J.; Chandler, M.T.; Kim, H.-S.; Son, J.; Son, S.-K.; Choi, S.K.; Baker, E.T. Widespread tectonic extension at the Central Indian Ridge between 8° S and 18° S. *Gondwana Res.* **2017**, *45*, 163–179. [CrossRef]
21. Fouquet, Y.; Cambon, P.; Etoubleau, J.; Charlou, J.L.; Ondréas, H.; Barriga, F.; Cherkashov, G.; Semkova, T.; Poroshina, I.; Bohn, M.; et al. Geodiversity of hydrothermal processes along the Mid-Atlantic Ridge and ultramafic-hosted mineralization: A new type of oceanic Cu-Zn-Co-Au volcanogenic massive sulfide deposit. *Large Igneous Prov.* **2010**, *188*, 321–367. [CrossRef]
22. Sauter, D.; Patriat, P.; Rommevaux-Jestin, C.; Cannat, M.; Briais, A.; Bergh, G.S.S.P.; Boulanger, D.; Deplus, C.; Grindlay, N.; Isezaki, N. The Southwest Indian Ridge between 49°15′ E and 57° E: Focused accretion and magma redistribution. *Earth Planet. Sci. Lett.* **2001**, *192*, 303–317. [CrossRef]
23. Wang, Y.; Han, X.; Zhou, Y.; Qiu, Z.; Yu, X.; Petersen, S.; Li, H.; Yang, M.; Chen, Y.; Liu, J.; et al. The Daxi Vent Field: An active mafic-hosted hydrothermal system at a non-transform offset on the slow-spreading Carlsberg Ridge, 6°48′ N. *Ore Geol. Rev.* **2021**, *129*, 103888. [CrossRef]
24. Dias, A.S.C.M.A.; Barriga, F. Mineralogy and geochemistry of hydrothermal sediments from the serpentinite-hosted Saldanha hydrothermal field (36°34′ N; 33°26′ W) at MAR. *Mar. Geol.* **2006**, *225*, 157–175. [CrossRef]
25. Cherkashov, G.; Kuznetsov, V.; Kuksa, K.; Tabuns, E.; Maksimov, F.; Bel'Tenev, V. Sulfide geochronology along the north-ern equatorial Mid-Atlantic Ridge. *Ore. Geol. Rev.* **2017**, *87*, 147–154. [CrossRef]
26. German, C.R.; Klinkhammer, G.P.; Rudnicki, M.D. The Rainbow hydrothermal plume, 36°15′ N., MAR. *Geophys. Res. Lett.* **1996**, *23*, 2979–2982. [CrossRef]
27. Melchert, B.; Devey, C.; German, C.; Lackschewitz, K.; Seifert, R.; Walter, M.; Mertens, C.; Yoerger, D.; Baker, E.; Paulick, H.; et al. First evidence for high-temperature off-axis venting of deep crustal/mantle heat: The Nibelungen hydrothermal field, southern Mid-Atlantic Ridge. *Earth Planet. Sci. Lett.* **2008**, *275*, 61–69. [CrossRef]
28. Sauter, D.; Cannat, M. The ultraslow spreading Southwest Indian Ridge. *Extrem. Events* **2010**, *188*, 153–173. [CrossRef]
29. Ding, T.; Tao, C.; Dias, A.A.; Liang, J.; Chen, J.; Wu, B.; Ma, D.; Zhang, R.; Wang, J.; Liao, S.; et al. Sulfur isotopic compositions of sulfides along the Southwest Indian Ridge: Implications for mineralization in ultramafic rocks. *Miner. Depos.* **2021**, *56*, 991–1006. [CrossRef]
30. Dick, H.J.B.; Lin, J.; Schouten, H. An ultraslow-spreading class of ocean ridge. *Nat. Cell Biol.* **2003**, *426*, 405–412. [CrossRef]
31. Cannat, M.; Rommevaux Jestin, C.; Sauter, D.; Deplus, C.; Mendel, V. Formation of the axial relief at the very slow spread-ing Southwest Indian Ridge (49° to 69° E). *J. Geophys. Res. Solid Earth* **1999**, *104*, 22825–22843. [CrossRef]
32. Behn, M.D.; Ito, G. Magmatic and tectonic extension at mid-ocean ridges: 1. Controls on fault characteristics. *Geochem. Geophys. Geosystems* **2008**, *9*, 9. [CrossRef]
33. Liu, C.; Li, J.; Tao, C.; Fan, Q.; Song, J.; Luo, Y.; Feng, B. Variations in faulting style of the Southwest Indian Ridge (46°–53.5° E): Implications for crustal accretion process at ultraslow-spreading ridges. *Tectonophysics* **2020**, *790*, 228552. [CrossRef]
34. Zhang, H. Tectonic Model and its Genetic Mechanism of Very-Low Spreading Ridges: Insight from Southwest Indian Ridge (46–52° E). Ph.D. Thesis, Peaking University, Beijing, China, 2017. (In Chinese).
35. Tao, C.; Li, H.; Deng, X.; Lei, J.; Wang, Y.; Zhang, K.; Zhou, J.; Liu, W. Hydrothermal Activity on ultraslow Spreading Ridge: New hydrothermal fields found on the Southwest Indian ridge. *AGU Fall Meet. Abstr.* **2014**, *2014*, S53C–S1061C.
36. Liu, C. Tectonic-Magmatic Characteristics of Southwest Indian Ridge 46~52.5° E and its Dynamic Formation Mechanism. Ph.D. Thesis, Peking University, Beijing, China, 2019. (In Chinese).

37. Tao, C.; Chen, S.; Baker, E.T.; Li, H.; Liang, J.; Liao, S.; Chen, Y.J.; Deng, X.; Zhang, G.; Gu, C.; et al. Hydrothermal plume mapping as a prospecting tool for seafloor sulfide deposits: A case study at the Zouyu-1 and Zouyu-2 hydrothermal fields in the southern Mid-Atlantic Ridge. *Mar. Geophys. Res.* **2017**, *38*, 3–16. [CrossRef]
38. Chen, S.; Tao, C.; German, C.R. Abundance of low-temperature axial venting at the equatorial East Pacific Rise. *Deep. Sea Res. Part I Oceanogr. Res. Pap.* **2021**, *167*, 103426. [CrossRef]
39. Yue, X.; Li, H.; Ren, J.; Tao, C.; Zhou, J.; Wang, Y.; Lü, X. Seafloor hydrothermal activity along mid-ocean ridge with strong melt supply: Study from segment 27, southwest Indian ridge. *Sci. Rep.* **2019**, *9*, 9874. [CrossRef]
40. Chen, S.; Tao, C.; Li, H.; Chen, Y.; Zhou, J.; Wu, T. A data processing method for MAPR hydrothermal plume turbidity data and its application in the Precious Stone Mountain hydrothermal field. *Acta Oceanol. Sin.* **2014**, *33*, 34–43. [CrossRef]
41. Goring, D.G.; Nikora, V.I. Despiking Acoustic Doppler Velocimeter Data. *J. Hydraul. Eng.* **2002**, *128*, 117–126. [CrossRef]
42. Walker, S.L.; Baker, E.T.; Resing, J.A.; Nakamura, K.; McLain, P.D. A new tool for detecting hydrothermal plumes: An ORP Sensor for the PMEL MAPR. *AGU Fall Meet. Abstr.* **2007**, *2007*, V21D–V753D.
43. Fraile-Nuez, E.; Santana-Casiano, J.M.; González-Dávila, M.; Vázquez, J.T.; Fernández-Salas, L.M.; Sánchez-Guillamón, O.; Palomino, D.; Presas-Navarro, C. Cyclic Behavior Associated with the Degassing Process at the Shallow Submarine Volcano Tagoro, Canary Islands, Spain. *Geosciences* **2018**, *8*, 457. [CrossRef]
44. Santana-Casiano, J.M.; Nuez, E.F.; Gonzalez-Davila, M.; Baker, E.T.; Resing, J.; Walker, S.L. Significant discharge of CO2 from hydrothermalism associated with the submarine volcano of El Hierro Island. *Sci. Rep.* **2016**, *6*, 25686. [CrossRef] [PubMed]
45. González-Vega, A.; Fraile-Nuez, E.; Santana-Casiano, J.M.; González-Dávila, M.; Escánez-Pérez, J.; Gómez-Ballesteros, M.; Tello, O.; Arrieta, J.M. Significant Release of Dissolved Inorganic Nutrients from the Shallow Submarine Volcano Tagoro (Canary Islands) Based on Seven-Year Monitoring. *Front. Mar. Sci.* **2020**, *6*, 829. [CrossRef]
46. Nuez, E.F.; Gonzalez-Davila, M.; Casiano, J.M.S.; Arístegui, J.; Alonso-González, I.J.; Hernández-León, S.; Blanco, M.J.; Rodriguez-Santana, A.; Hernández-Guerra, A.; Gelado-Caballero, M.; et al. The submarine volcano eruption at the island of El Hierro: Physical-chemical perturbation and biological response. *Sci. Rep.* **2012**, *2*, 486. [CrossRef] [PubMed]
47. Haymon, R.M.; White, S.M.; Baker, E.T.; Anderson, P.G.; Macdonald, K.C.; Resing, J. High-resolution surveys along the hot spot-affected Gálapagos Spreading Center: 3. Black smoker discoveries and the implications for geological controls on hydrothermal activity. *Geochem. Geophys. Geosystems* **2008**, *9*, 9. [CrossRef]
48. Baker, E.T.; German, C.R.; Elderfield, H. Hydrothermal plumes over spreading-center axes: Global distributions and geo-logical inferences. *Geophys. Monogr. Am. Geophys. Union* **1995**, *91*, 47.
49. German, C.R.; Bennett, S.A.; Connelly, D.P.; Evans, A.J.; Murton, B.J.; Parson, L.M.; Prien, R.D.; Ramirez-Llodra, E.; Jakuba, M.; Shank, T.M. Hydrothermal activity on the southern Mid-Atlantic Ridge: Tectonically-and volcanically-controlled vent-ing at 4–5 S. *Earth Planet. Sci. Lett.* **2008**, *273*, 332–344. [CrossRef]
50. Tao, C.; Seyfried, W.E.J.; Lowell, R.P.; Liu, Y.; Liang, J.; Guo, Z.; Ding, K.; Zhang, H.; Liu, J.; Qiu, L.; et al. Deep high-temperature hydrothermal circulation in a detachment faulting system on the ultra-slow spreading ridge. *Nat. Commun.* **2020**, *11*, 1300. [CrossRef]
51. Liao, S.; Tao, C.; Li, H.; Zhang, G.; Liang, J.; Yang, W.; Wang, Y. Surface sediment geochemistry and hydrothermal activity indicators in the Dragon Horn area on the Southwest Indian Ridge. *Mar. Geol.* **2018**, *398*, 22–34. [CrossRef]
52. Baker, E.T.; Haymon, R.M.; Resing, J.A.; White, S.M.; Walker, S.L.; Macdonald, K.C.; Nakamura, K.I. High-resolution surveys along the hot spot–affected Galápagos Spreading Center: 1. Distribution of hydrothermal activity. *Geochem. Geophys. Geosystems* **2008**, *9*, 1–16. [CrossRef]
53. German, C.R.; Bowen, A.; Coleman, M.; Honig, D.L.; Huber, J.; Jakuba, M.V.; Kinsey, J.C.; Kurz, M.; Leroy, S.; McDermott, J.M.; et al. Diverse styles of submarine venting on the ultraslow spreading Mid-Cayman Rise. *Proc. Natl. Acad. Sci. USA* **2010**, *107*, 14020–14025. [CrossRef]
54. Schmale, O.; Walter, M.; Schneider Von Deimling, J.; Sültenfuß, J.; Walker, S.; Rehder, G.; Keir, R. Fluid and gas fluxes from the Logatchev hydrothermal vent area. *Geochem. Geophys. Geosystems* **2012**, *13*, 1–12. [CrossRef]
55. Tao, C.; Wu, G.; Ni, J.; Zhao, H.; Su, X.; Zhou, N.; Li, J.; Chen, Y.J.; Cui, R.; Deng, X. New hydrothermal fields found along the SWIR during the Legs 5-7 of the Chinese DY115-20 Expedition. *AGU Fall Meet. Abstr.* **2009**, *2009*, S21A–S1150A.
56. Chen, J.; Tao, C.; Liang, J.; Liao, S.; Dong, C.; Li, H.; Li, W.; Wang, Y.; Yue, X.; He, Y. Newly discovered hydrothermal fields along the ultraslow-spreading Southwest Indian Ridge around 63° E. *Acta Oceanol. Sin.* **2018**, *37*, 61–67. [CrossRef]
57. Münch, U.; Lalou, C.; Halbach, P.; Fujimoto, H. Relict hydrothermal events along the super-slow Southwest Indian spread-ing ridge near 63° 56′ E—Mineralogy, chemistry and chronology of sulfide samples. *Chem. Geol.* **2001**, *177*, 341–349. [CrossRef]
58. Liao, S.; Tao, C.; Li, H.; Barriga, F.J.; Liang, J.; Yang, W.; Yu, J.; Zhu, C. Bulk geochemistry, sulfur isotope characteristics of the Yuhuang-1 hydrothermal field on the ultraslow-spreading Southwest Indian Ridge. *Ore. Geol. Rev.* **2018**, *96*, 13–27. [CrossRef]
59. Bemis, K.; Lowell, R.; Farough, A. Diffuse Flow on and Around Hydrothermal Vents at Mid-Ocean Ridges. *Oceanography* **2012**, *25*, 182–191. [CrossRef]
60. Devey, C.W.; German, C.R.; Haase, K.M.; Lackschewitz, K.S.; Melchert, B.; Connelly, D.P. The Relationships Between Volcanism, Tectonism, and Hydrothermal Activity on the Southern Equatorial Mid-Atlantic Ridge. In *Diversity of Hydrothermal Systems on Slow Spreading Ocean Ridges*; American Geophysical Union: Washington, DC, USA, 2010; Volume 188, pp. 133–152.
61. Haymon, R.M.; White, S.M. Fine-scale segmentation of volcanic/hydrothermal systems along fast-spreading ridge crests. *Earth Planet. Sci. Lett.* **2004**, *226*, 367–382. [CrossRef]

62. Haymon, R.M.; Fornari, D.J.; Edwards, M.H.; Carbotte, S.; Wright, D.; Macdonald, K.C. Hydrothermal vent distribution along the East Pacific Rise crest (9 09′–54′ N) and its relationship to magmatic and tectonic processes on fast-spreading mid-ocean ridges. *Earth Planet. Sci. Lett.* **1991**, *104*, 513–534. [CrossRef]
63. Haase, K.; Koschinsky, A.; Petersen, S.; Devey, C.; German, C.; Lackschewitz, K.; Melchert, B.; Seifert, R.; Borowski, C.; Giere, O.; et al. Diking, young volcanism and diffuse hydrothermal activity on the southern Mid-Atlantic Ridge: The Lilliput field at 9°33′ S. *Mar. Geol.* **2009**, *266*, 52–64. [CrossRef]
64. Kim, J.; Son, S.; Kim, D.; Pak, S.; Yu, O.H.; Walker, S.L.; Oh, J.; Choi, S.K.; Ra, K.; Ko, Y.; et al. Discovery of Active Hydrothermal Vent Fields Along the Central Indian Ridge, 8–12° S. *Geochem. Geophys. Geosystems* **2020**, *21*, e2020G–e9058G. [CrossRef]
65. Li, B.; Shi, X.; Wang, S.; Wang, J.; Yan, Q. Mafic-hosted seafloor sulfide mineralization at the margin of a non-transform dis-continuity on the southern mid-Atlantic ridge. *Mar. Georesour. Geotechnol.* **2019**, *37*, 727–738. [CrossRef]
66. Standish, J.J.; Dick, H.J.; Michael, P.J.; Melson, W.G.; O'Hearn, T. MORB generation beneath the ultraslow spreading South-west Indian Ridge (9–25 E): Major element chemistry and the importance of process versus source. *Geochem. Geophys. Geosystems* **2008**, *9*, 1–39. [CrossRef]
67. Standish, J.J.; Sims, K.W.W. Young off-axis volcanism along the ultraslow-spreading Southwest Indian Ridge. *Nat. Geosci.* **2010**, *3*, 286–292. [CrossRef]
68. Buck, W.R.; Lavier, L.L.; Poliakov, A.N.B. Modes of faulting at mid-ocean ridges. *Nat. Cell Biol.* **2005**, *434*, 719–723. [CrossRef] [PubMed]
69. Lowell, R.P. Hydrothermal circulation at slow spreading ridges: Analysis of heat sources and heat transfer processes. *Extrem. Events* **2010**, *188*, 11–26. [CrossRef]
70. Dick, H.J.; Natland, J.H.; Alt, J.C.; Bach, W.; Bideau, D.; Gee, J.; Haggas, S.; Hertogen, J.G.; Hirth, G.; Holm, P.M.; et al. A long in situ section of the lower ocean crust: Results of ODP Leg 176 drilling at the Southwest Indian Ridge. *Earth Planet. Sci. Lett.* **2000**, *179*, 31–51. [CrossRef]
71. Kelemen, P.B.; Kikawa, E.; Miller, D.J.; Party, S.S. Leg 209 Summary: Processes in a 20-km-thick Conductive Boundary Layer Beneath the Mid-Atlantic Ridge, 14–16 N. In *Proceedings of the Ocean Drilling Program, Scientific Results*; Ocean Drilling Program: College Station, TX, USA, 2007; pp. 1–33.
72. Tao, C.; Li, J. *Atlas of Multidisciplinary Comprehensive Research on the Southwest Indian Ocean Polymetallic Sulfide Contract Area and Adjacent Areas*; Science Press: Beijing, China, 2021; pp. 1–81. (In Chinese)
73. Zhang, H.-T.; Li, J.-H.; Tao, C.-H. Discussions on the bathymetric segmentation and tectonogenesis of the oblique spreading South-west Indian Ridge. *Earth Sci. Front.* **2021**, *28*, 271.
74. Han, X.; Wu, G.; Cui, R.; Qiu, Z.; Deng, X.; Wang, Y.; Dy, S.P.O.; Leg, C. Discovery of a hydrothermal sulfide deposit on the Southwest Indian Ridge at 49.2° E. *AGU Fall Meet. Abstr.* **2010**, *2010*, S21C–S1531C.